

GaRLIO: Gravity enhanced Radar-LiDAR-Inertial Odometry

Chiyun Noh¹, Wooseong Yang¹, Minwoo Jung¹, Sangwoo Jung¹ and Ayoung Kim^{1*}

Abstract—Recently, gravity has been highlighted as a crucial constraint for state estimation to alleviate potential vertical drift. Existing online gravity estimation methods rely on pose estimation combined with IMU measurements, which is considered best practice when direct velocity measurements are unavailable. However, with radar sensors providing direct velocity data—a measurement not yet utilized for gravity estimation—we found a significant opportunity to improve gravity estimation accuracy substantially. GaRLIO, the proposed gravity-enhanced Radar-LiDAR-Inertial Odometry, can robustly predict gravity to reduce vertical drift while simultaneously enhancing state estimation performance using pointwise velocity measurements. Furthermore, GaRLIO ensures robustness in dynamic environments by utilizing radar to remove dynamic objects from LiDAR point clouds. Our method is validated through experiments in various environments prone to vertical drift, demonstrating superior performance compared to traditional LiDAR-Inertial Odometry methods. We make our source code publicly available to encourage further research and development. <https://github.com/ChiyunNoh/GaRLIO>

I. INTRODUCTION

Range-based sensor simultaneous localization and mapping (SLAM) is widely used for precise pose estimation of mobile robots in unknown environments. Along with many of range sensors, Light Detection and Ranging (LiDAR) has drawn attention for its intuitive spatial information, especially being integrated with inertial measurement unit (IMU) to exhibit high precision and robustness [1–3]. However, due to the sparse vertical resolution and remaining uncertainties in LiDAR measurements [4], LiDAR-Inertial Odometry (LIO) is still susceptible to vertical drift.

In this context, exploiting gravity shows promising performance in mitigating vertical drift from recent works [5–9]. Since gravity maintains size and direction constant across diverse conditions, precise local gravity estimation allows for an accurate rotation calculation between the global and body frame. To be more specific, accurate gravity estimation may lead to reliable observation of roll and pitch, reducing the vertical position error. Most existing methods measure gravity vector relying on the relationship between IMU acceleration measurements and estimated pose [6–8] or only when the robot motion is stationary [9]. However, establishing the relationship between pose and acceleration generally results in amplified errors due to the double integrated bias and noise of the IMU acceleration [10].

Since traditional LIO lacks direct velocity observations at the raw measurement level, they rely on pose estimation

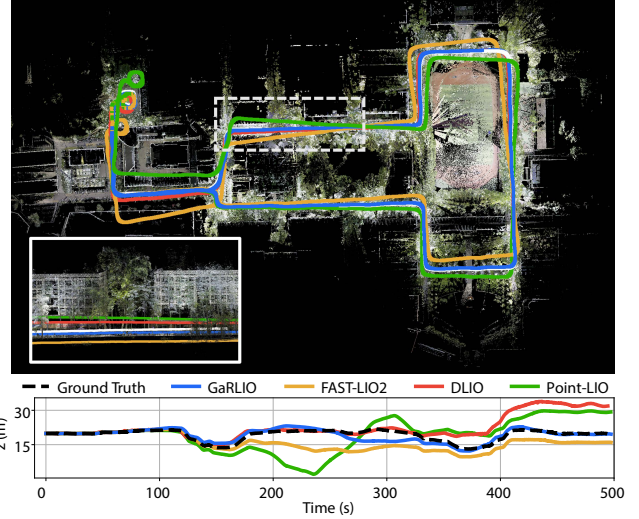


Fig. 1: **Top:** Trajectories of GaRLIO and other methods with ground truth (white) overlaid on the terrestrial laser scanner (TLS) map. **Bottom:** Elevation plot along path length. Our method (blue) reported only 1.21 m vertical mean error over 2.045 km path length.

and IMU measurements to estimate gravity. Yet, we observe that incorporating velocity measurements can significantly enhance the accuracy of gravity estimation. While one study has explored the fusion of radar with LIO to improve state estimation performance by providing velocity measurements [11], no existing work has integrated velocity measurements specifically for the purpose of gravity estimation.

In this paper, we propose GaRLIO, a gravity-enhanced Radar-LiDAR-Inertial Odometry that introduces a novel idea of exploiting radar for gravity estimation. GaRLIO integrates a new gravity estimation technique that leverages radar Doppler measurements to address vertical drift and inaccuracy. Integrating radar with LIO improves velocity estimation accuracy, allowing for more precise local gravity estimation, which reduces vertical drift. Furthermore, this integration facilitates the dynamic object filtering in LiDAR point cloud, ensuring performance in diverse environments. GaRLIO is evaluated on public datasets with various challenging scenarios, including downhill conditions where vertical drift prevalently occurs in LIO, exhibiting surpassing performance compared with state-of-the-art (SOTA) methods. The pipeline of our method is as shown in Fig. 2. Our contributions are as follows:

- We propose GaRLIO that utilizes gravity to address the vertical drift of LIO. GaRLIO introduces a novel velocity-aware gravity estimation that leverages radar Doppler measurements to reduce vertical drift and inaccuracy common in velocity-ignorant approaches. To our knowledge, this is the first method using radar velocity

¹C. Noh, W. Yang, M. Jung, S. Jung and A. Kim are with the Dept. of Mechanical Engineering, SNU, Seoul, S. Korea [gch06208, yellowish, moonshot, dan0130, ayoungk]@snu.ac.kr

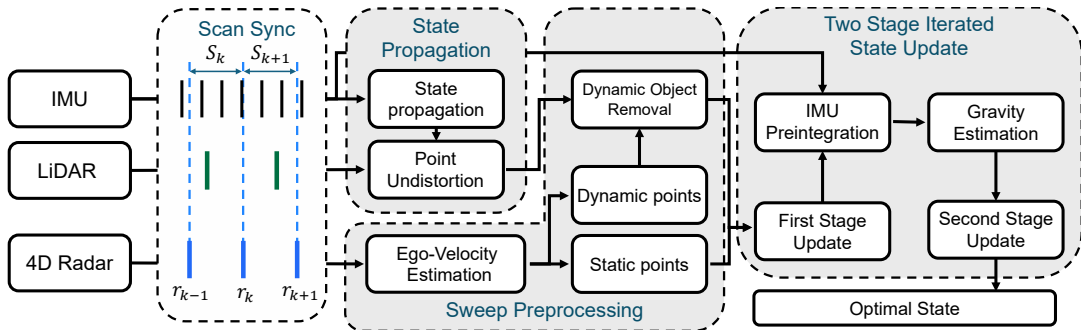


Fig. 2: GaRLIO is divided into four primary modules. Each module contributes to achieving the optimal state by removing LiDAR dynamic points and calculating both pointwise velocity and velocity-aware gravity residuals.

to estimate gravity.

- GaRLIO fuses radar with LIO and demonstrated enhanced state estimation performance by exploiting pointwise velocity residuals based on radar measurements. Additionally, our fusion approach effectively removes dynamic points within LiDAR point clouds.
- GaRLIO is evaluated on public datasets with challenging scenarios, including downhill, where the introduced residuals demonstrated performance improvement. We open-source GaRLIO to encourage further development in radar-LiDAR-IMU fusion.

II. RELATED WORK

A. LiDAR and Radar Fusion

Radar and LiDAR are complementary range sensors, prompting numerous studies on their fusion for localization [12–14]. Ma et al. [12] and Park et al. [13] leveraged a LiDAR map to align radar scans, enabling robust localization in adverse conditions as smoke or fog. However, they heavily depend on an accurate LiDAR map, underscoring the importance of combining both sensors for precise SLAM.

Despite the significance of sensor fusion, LiDAR and radar fusion for SLAM remains uncommon. Even though DR-LRIO [11] proposed a tightly-coupled method between Frequency Modulated Continuous Wave (FMCW) radar and LiDAR to enhance localization in challenging environments, it still contends with inherent uncertainties of radar, particularly along the z -axis. Our method expands the application of radar data beyond ego-velocity estimation by introducing additional strategies, such as dynamic object filtering and gravity estimation, to further improve SLAM performance.

B. Gravity Estimation in LiDAR-Inertial Odometry

Accurate gravity estimation is essential in LIO since IMU acceleration measurements include gravity. Additionally, aligning maps based on the gravity vector alleviates vertical drift. The most common approach for predicting gravity involves probabilistic methods [1, 2]. However, these studies did not focus on exploiting gravity for state updates or map alignment. Recent works directly impose gravity as new constraints to mitigate vertical drift. Nebula [9] measured gravity using IMU acceleration only when the robot is stationary, introducing a gravity factor to constrain roll and pitch. D-LIOM [6] and Wildcat [8] estimated gravity

using IMU measurements and odometry, incorporating gravity alignment constraints. Additionally, Nemiroff et al. [7] jointly optimized accelerometer intrinsics and gravity. These methods partially tackled vertical drift; however, relying on velocity-ignorant models for gravity estimations. The velocity-ignorant model focuses on the relationship between IMU acceleration and the pose, which impedes accurate gravity estimation due to errors exacerbated by double integration. To tackle these issues, we incorporate radar-based velocity residuals and velocity-aware gravity residuals into LIO, eliminating the necessity of double integration.

III. PRELIMINARY

A. Notation

In this paper, x_k^j denotes the j th iteration of Kalman filter update for k th state, and $(\cdot), (\hat{\cdot}), (\bar{\cdot})$ denote ground truth, propagated, and optimal state. Global frame $^G(\cdot)$ is set as initial IMU frame, while $^A(\cdot)$ denote sensor frames. The state description and definition of \boxplus/\boxminus are as follows:

$$\begin{aligned}
 \mathcal{M} &\triangleq SE_2(3) \times \mathbb{R}^6, \quad \mathbf{x} \triangleq [\mathcal{X}^T, \mathbf{b}_\omega^T, \mathbf{b}_a^T]^T \in \mathcal{M} \\
 \mathbf{u} &\triangleq \begin{bmatrix} \omega_m^T & a_m^T \end{bmatrix}^T, \quad \mathbf{n} \triangleq \begin{bmatrix} n_\omega^T & n_a^T & n_{b_\omega}^T & n_{b_a}^T \end{bmatrix}^T \quad (1) \\
 \mathcal{X} &\triangleq \begin{bmatrix} {}^G\mathbf{R}_I & {}^G\mathbf{v}_I & {}^G\mathbf{p}_I \\ 0 & 1 & 0 \\ 0 & 0 & 1 \end{bmatrix} \in SE_2(3) \\
 \delta\hat{\mathbf{x}}_k &\triangleq \mathbf{x}_k \boxminus \hat{\mathbf{x}}_k = \begin{bmatrix} \delta\hat{\theta}_k, \delta\hat{\mathbf{v}}_k, \delta\hat{\mathbf{p}}_k, \delta\hat{\mathbf{b}}_{\omega_k}, \delta\hat{\mathbf{b}}_{a_k} \end{bmatrix} \\
 &= \begin{bmatrix} \text{Log}(\mathcal{X}_k \hat{\mathcal{X}}_k^{-1}), \mathbf{b}_{\omega_k} - \hat{\mathbf{b}}_{\omega_k}, \mathbf{b}_{a_k} - \hat{\mathbf{b}}_{a_k} \end{bmatrix} \in \mathbb{R}^{15} \\
 \mathbf{x} \boxplus \delta\hat{\mathbf{x}} &= \begin{bmatrix} \mathcal{X} \\ \mathbf{b} \end{bmatrix} \boxplus \begin{bmatrix} \xi \\ \hat{\mathbf{b}} \end{bmatrix} \triangleq \begin{bmatrix} \text{Exp}(\xi) \cdot \mathcal{X} \\ \mathbf{b} + \hat{\mathbf{b}} \end{bmatrix}
 \end{aligned}$$

, where $\mathbf{b}, \hat{\mathbf{b}} \in \mathbb{R}^6$ and $\xi \in \mathbb{R}^9$. In (1), ${}^G\mathbf{R}_I$, ${}^G\mathbf{v}_I$, and ${}^G\mathbf{p}_I$ denote the rotation, velocity, and position of the IMU in the global frame, while \mathbf{b} represents the IMU bias. The angular velocity and linear acceleration from the IMU are denoted by ω_m and a_m , with \mathbf{n} representing the Gaussian white noise associated with these measurements and biases.

B. State Propagation

For state prediction within the time interval $[k, k+1]$, we discretize the continuous-time IMU kinematic model using a zero-order holder with an IMU sampling period Δt [1]. The resulting discretized motion model \mathbf{f} , is formulated as:

$$\mathbf{x}_{i+1} = \mathbf{x}_i \boxplus (\Delta t \mathbf{f}(\mathbf{x}_i, \mathbf{u}_i, \mathbf{n}_i)), \quad (2)$$

$$\mathbf{f}(\mathbf{x}_i, \mathbf{u}_i, \mathbf{n}_i) = \begin{bmatrix} \omega_{m_i} - b_{\omega_i} - n_{\omega_i} \\ {}^G \mathbf{R}_{I_i} (a_{m_i} - b_{a_i} - n_{a_i}) + {}^G \mathbf{g}_i \\ {}^G \mathbf{v}_{I_i} + \frac{1}{2} ({}^G \mathbf{R}_{I_i} (a_{m_i} - b_{a_i} - n_{a_i}) + {}^G \mathbf{g}_i) \Delta t \\ n_{b_{\omega_i}} \\ n_{b_{a_i}} \end{bmatrix}$$

State prediction is conducted using the discrete IMU kinematic model from (2) by setting the noise term $\mathbf{n} = 0$:

$$\hat{\mathbf{x}}_{\tau+1} = \hat{\mathbf{x}}_{\tau} \boxplus (\Delta t \mathbf{f}(\hat{\mathbf{x}}_{\tau}, \mathbf{u}_{\tau}, 0)); \quad t_k \leq t_{\tau} < t_{k+1} \quad (3)$$

C. Error State Prediction

To ensure the system depends on the error rather than the state, we define the error using a right-invariant error [15]. The error-state transition matrix is derived by combining the error state (1) with the IMU motion model (2). The error-state $\delta \hat{\mathbf{x}}_{\tau+1}$ and its covariance $\hat{\mathbf{P}}_{\tau+1}$ are then computed as:

$$\begin{aligned} \delta \hat{\mathbf{x}}_{\tau+1} &= \mathbf{x}_{\tau+1} - \hat{\mathbf{x}}_{\tau+1} \simeq \mathbf{F}_{\delta \hat{\mathbf{x}}_{\tau}} \delta \hat{\mathbf{x}}_{\tau} + \mathbf{F}_{\mathbf{n}_{\tau}} \mathbf{n}_{\tau} \\ \hat{\mathbf{P}}_{\tau+1} &= \mathbf{F}_{\delta \hat{\mathbf{x}}_{\tau}} \hat{\mathbf{P}}_{\tau} \mathbf{F}_{\delta \hat{\mathbf{x}}_{\tau}}^T + \mathbf{F}_{\mathbf{n}_{\tau}} \mathbf{Q}_{\tau} \mathbf{F}_{\mathbf{n}_{\tau}}^T \end{aligned} \quad (4)$$

The initial value of $\delta \hat{\mathbf{x}}_i$ is set to zero. $\mathbf{F}_{\delta \hat{\mathbf{x}}_{\tau}}$ and $\mathbf{F}_{\mathbf{n}_{\tau}}$ denote the Jacobian matrix of $\delta \hat{\mathbf{x}}_{\tau+1}$ with respect to $\delta \hat{\mathbf{x}}_{\tau}$ evaluated under the condition that $\delta \hat{\mathbf{x}}_{\tau} = 0$ and $\mathbf{n}_{\tau} = 0$.

D. Iterated State Update

The state $\hat{\mathbf{x}}_{k+1}$ and covariance $\hat{\mathbf{P}}_{k+1}$ are used as the prior distribution of \mathbf{x}_{k+1} . With the measurement at time index $k+1$ serving as the observation, the posterior distribution of the state can be determined [16]. Using the prior distribution, the error state propagation can be performed as follows:

$$\begin{aligned} \delta \hat{\mathbf{x}}_{k+1} &= (\hat{\mathbf{x}}_{k+1}^j \boxminus \hat{\mathbf{x}}_{k+1}) + \mathbf{J}_{k+1} \delta \mathbf{x}_j \\ \delta \mathbf{x}_j &\sim \mathcal{N}(-\mathbf{J}_{k+1}^{-1} (\hat{\mathbf{x}}_{k+1}^j \boxminus \hat{\mathbf{x}}_{k+1}), \mathbf{J}_{k+1}^{-1} \hat{\mathbf{P}}_{k+1} \mathbf{J}_{k+1}^{-T}) \end{aligned} \quad (5)$$

\mathbf{J}_{k+1} is the Jacobian of $\delta \hat{\mathbf{x}}_{k+1}$ w.r.t $\delta \mathbf{x}_j$ at 0, and detailed derivation is in [17]. After project $\hat{\mathbf{x}}_{k+1}^j$ to the same space of $\delta \mathbf{x}_j$, we can get an optimal $\delta \mathbf{x}_j$ combining (5) and measurement model $z_{k+1}^M = \mathbf{h}_{M^j}(\mathbf{x}_k, \mathbf{v}_j^M)$:

$$\min_{\delta \mathbf{x}_j} (\|\mathbf{x}_{k+1} \boxminus \hat{\mathbf{x}}_{k+1}\|_{\mathbf{P}}^2 + \sum_M \sum_{j=1}^{|M|} \|\mathbf{r}_{M^j} + \mathbf{H}_{M^j} \delta \hat{\mathbf{x}}_k\|_{R_j^M}^2) \quad (6)$$

where $\mathbf{P} = \mathbf{J}_{k+1}^{-1} \hat{\mathbf{P}}_{k+1} \mathbf{J}_{k+1}^{-T}$, \mathbf{H}_{M^j} is the Jacobian matrix of \mathbf{h}_{M^j} w.r.t $\delta \hat{\mathbf{x}}_k$ and measurement model which is used in this paper is described in §IV-C and §IV-D. The δx_j that minimizes equation (6) can be obtained through the Kalman filter update process using $\mathbf{H} = [\mathbf{H}_{M^1}, \dots]$, $\mathbf{R} = \text{diag} [R_1^M, \dots]$. If the state converges, the optimal state $\bar{\mathbf{x}}_{k+1}$ and covariance $\bar{\mathbf{P}}_{k+1}$ are updated and details are in [16].

IV. GRAVITY-ENHANCED RADAR-LiDAR FUSION

A. Radar-LiDAR Scan Synchronization

Since 4D radar operates at a higher frequency than LiDAR, we utilized sweep reconstruction [18] to synchronize the end timestamp of LiDAR and radar, using the radar's timestamp r_k . A sweep S_{k+1} is constructed using LiDAR points and IMU measurements recorded between r_k and r_{k+1} , along with radar captured at r_{k+1} . To address possible missing

segments in the radar-based sweep reconstruction, we filled in missing field of view (FOV) sections of S_{k+1} with data from the previous sweep S_k to generate a complete LiDAR scan. Once the sweep S_{k+1} is constructed, state propagation is performed using IMU measurements as (3). LiDAR points in S_{k+1} are subsequently corrected with motion compensation to be transformed into the $(\cdot)^{r_{k+1}}$ frame.

B. Radar-guided LiDAR Sweep Preprocessing

Before the sweep S_{k+1} is utilized for the update module, a preprocessing step is conducted to remove dynamic points from the sweep based on radar Doppler measurements.

1) *Radar Point Cloud Pre-processing*: The 4D radar provides both 3D points and Doppler velocities, enabling it to compute 3D ego velocity in the $(\cdot)^{r_k}$ frame through the 3-Point RANSAC-LSQ method [19]. With this velocity, radar can filter out moving objects within a single frame without needing sequential data. This filtering segments the radar point cloud into static points, ${}^R P_s$, and dynamic points, ${}^R P_d$, which include both moving objects and noise.

2) *Dynamic Removal in LiDAR*: Dynamic points ${}^R P_d$ are exploited to remove dynamic points from the LiDAR point cloud, ${}^L P$. However, due to the higher uncertainty in the z -direction and sparser nature of the radar point cloud used in this work, compared to the LiDAR point cloud, establishing precise point correspondences becomes challenging.

To overcome this, we projected both the LiDAR and radar dynamic point clouds onto the xy plane and compared the two in 2D space. Using the pointwise uncertainty matrix Σ_{r_i} [20], we computed the Mahalanobis distance between each LiDAR point and the radar dynamic point as follows:

$$d = (P_{XY} ({}^R p_i - {}^R \mathbf{T}_L {}^L p_j))^T \bar{\Sigma}_{r_i} (P_{XY} ({}^R p_i - {}^R \mathbf{T}_L {}^L p_j)), \quad (7)$$

where P_{XY} is the projection matrix on xy plane, $\bar{\Sigma}_{r_i} = P_{XY} \Sigma_{r_i} P_{XY}^T$, ${}^R p_i \in {}^R P_d$, ${}^L p_j \in {}^L P$. LiDAR points within a threshold $d < \epsilon$ are considered dynamic and filtered out.

C. Pointwise Residuals for First Stage Update

In the first stage update, radar and LiDAR measurements are integrated to update the state using pointwise residuals.

1) *Point-to-Plane Residual*: The residual is calculated using the dynamic-removed LiDAR point cloud, ${}^L P_{k+1}$, obtained from §IV-B. Each point ${}^L p_j$ in ${}^L P_{k+1}$ is first transformed into the global frame. Then, five neighboring points are selected for each point using an ikd-tree [21], and the residual for each point is computed as follows:

$$\mathbf{h}_{L^j}(\mathbf{x}_k, \mathbf{v}_j^L) = {}^G u_j^T ({}^G \mathbf{R}_{I_k} ({}^I \mathbf{R}_L ({}^L p_j + \mathbf{v}_j^L) + {}^I p_L) + {}^G p_{I_k} - {}^G q_j), \quad (8)$$

where ${}^I \mathbf{R}_L$, ${}^I p_L$ are LiDAR-IMU extrinsic parameter, ${}^G q_j$ is the centroid of five points, ${}^G u_j$ is their normal vector and \mathbf{v}_j^L is a measurement noise of LiDAR. Based on the residuals in (8), the Jacobian matrix of \mathbf{h}_{L^j} w.r.t $\delta \hat{\mathbf{x}}_k$, \mathbf{H}_{L^j} is computed according to the definition of the invariant error:

$$\begin{aligned} \mathbf{H}_{L^j} &= {}^G u_j^T \left[-[{}^G p_j]_{\times} \quad \mathbf{0} \quad \mathbf{I} \quad \mathbf{0} \quad \mathbf{0} \right] \\ \mathbf{r}_{L^j} + \mathbf{H}_{L^j} \delta \hat{\mathbf{x}}_k &\sim \mathcal{N}(0, R_j^L) \end{aligned} \quad (9)$$

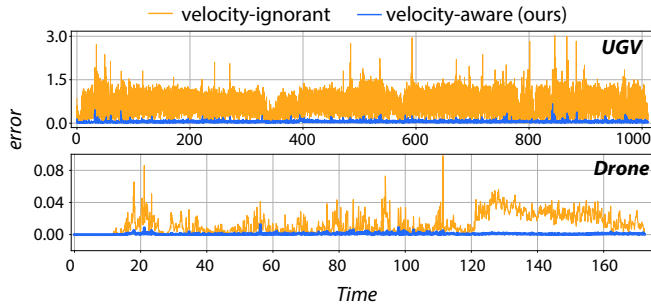


Fig. 3: Gravity estimation using the velocity-ignorant (yellow) and velocity-aware method (ours, blue) on different platforms.

where ${}^G p_j$ is LiDAR point in global frame and we set R_j^L as the same value.

2) *Pointwise Velocity Residual*: The static radar points ${}^R p_j$ are exploited as measurements to compute the velocity residual. The pointwise velocity residual is as follows:

$$\begin{aligned} \mathbf{h}_{Rj}(\mathbf{x}_k, \mathbf{v}_j^R) &= \mathbf{u}({}^R p_j)^\top {}^G \hat{\mathbf{v}}_R - {}^R \mathbf{v}_{m,j} \\ &= \mathbf{u}({}^R p_j)^\top {}^I \mathbf{R}_R^\top \left({}^G \mathbf{R}_{I_k} {}^G \mathbf{v}_I + [\omega_I]_\times {}^I p_R \right) - {}^R \mathbf{v}_{m,j} \end{aligned} \quad (10)$$

where ${}^I \mathbf{R}_R$ and ${}^I p_R$ are the radar-IMU extrinsic parameters, and ${}^R \mathbf{v}_{m,j}$ is the Doppler measurement at point ${}^R p_j$. The function $\mathbf{u}(\cdot)$ represents the unit vector.

Since static radar points may still contain outliers, each static point's uncertainty is assessed using the modified z-score M_j , which is based on deviation between ${}^R \mathbf{v}_{m,j}$ and the estimated ego velocity from §IV-B. Utilizing these residuals and uncertainties, the Jacobian of the pointwise velocity residual can be computed as follows:

$$\begin{aligned} \mathbf{H}_{Rj} &= \mathbf{u}({}^R p_j)^\top {}^I \mathbf{R}_R^\top \begin{bmatrix} \mathbf{0} & {}^G \hat{\mathbf{R}}_{I_k}^\top & \mathbf{0} & [{}^I p_R]_\times & \mathbf{0} \end{bmatrix} \\ \mathbf{r}_{Rj} + \mathbf{H}_{Rj} \delta \hat{\mathbf{x}}_k &= -n_{R,j} \sim \mathcal{N}(0, R_j^R) \\ R_j^R &= \begin{cases} R_v + \alpha M_j & \text{if } |M_j| > 3.5 \\ R_v & \text{otherwise} \end{cases} \end{aligned} \quad (11)$$

By incorporating two residuals, the state is updated according to (6), where M includes L and R . The optimal state $\hat{\mathbf{x}}_{k+1}^1$ and covariance $\hat{\mathbf{P}}_{k+1}^1$ from the first stage update are then utilized in the second stage along with the gravity residual.

D. Gravity Residual for Second Stage Update

As will be shown in this paper, incorporating radar velocity measurements into LIO effectively enhances the state estimation. Furthermore, the velocity-aware approach enables more precise local gravity estimation using the optimal state of first update. By utilizing the IMU preintegration with estimated biases, a velocity constraint β_{k+1}^k for the time interval can be derived as follows [22]:

$$\beta_{k+1}^k = \int_{t \in [r_k, r_{k+1})} {}^{I_k} \mathbf{R}_{I_t} (\hat{a}_t - \hat{b}_{a_t}) dt, \quad (12)$$

where subscript I_t denotes the IMU frame at index t . Using β_{k+1}^k , we can establish the relationship between IMU acceleration measurement and estimated velocity which was updated with radar measurements:

$$\beta_{k+1}^k = {}^{I_k} \mathbf{R}_{I_{k+1}} {}^{I_{k+1}} \mathbf{v}_{I_{k+1}} + {}^{I_k} \mathbf{g} \Delta t - {}^{I_k} \mathbf{v}_{I_k} \quad (13)$$

When solving for gravity \mathbf{g} and expressing it in terms of the state, it can be written as follows:

TABLE I: Effect of Velocity Measurement on Gravity Estimation Evaluated on Car Sequences from the NTU4DRadLM and Snail-Radar Datasets.

| | <i>loop2</i> | | <i>if</i> | | <i>sl</i> | |
|---------|--------------|--------------|--------------|--------------|--------------|--------------|
| | mean | std | mean | std | mean | std |
| w/ vel | 0.035 | 0.053 | 0.036 | 0.030 | 0.164 | 0.123 |
| w/o vel | 0.037 | 0.055 | 0.043 | 0.031 | 0.167 | 0.123 |

$$\begin{aligned} {}^{I_k} \hat{\mathbf{g}} &= \frac{\beta_{k+1}^k - {}^G \hat{\mathbf{R}}_{I_k}^\top {}^G \hat{\mathbf{R}}_{I_{k+1}} {}^G \hat{\mathbf{R}}_{I_{k+1}}^\top {}^G \hat{\mathbf{v}}_{I_{k+1}} + {}^G \hat{\mathbf{R}}_{I_k}^\top {}^G \hat{\mathbf{v}}_{I_k}}{\Delta t} \\ {}^G \hat{\mathbf{g}} &= {}^G \hat{\mathbf{R}}_{I_k} {}^{I_k} \hat{\mathbf{g}} = \frac{{}^G \hat{\mathbf{R}}_{I_k} \beta_{k+1}^k - {}^G \hat{\mathbf{v}}_{I_{k+1}} + {}^G \hat{\mathbf{v}}_{I_k}}{\Delta t} \end{aligned} \quad (14)$$

World frame gravity ${}^G \mathbf{g}$ is calculated through static initialization using IMU acceleration. By calculating the residual between ${}^G \mathbf{g}$ and the predicted gravity ${}^G \hat{\mathbf{g}}_r$ on the \mathcal{S}^2 manifold from ${}^G \hat{\mathbf{g}} \in \mathbb{R}^3$, compensating the deviation of roll and pitch directions is possible. Gravity residual is defined using cosine similarity, and its Jacobian is represented as follows:

$$\begin{aligned} \mathbf{h}_g(\mathbf{x}_k, \mathbf{v}_k^g) &= 1 - {}^G \mathbf{g}^\top {}^G \hat{\mathbf{g}}_r(\mathbf{x}_k, \mathbf{v}_k^g) = \mathbf{h}_g(\hat{\mathbf{x}}_k, 0) + \mathbf{H}_g \delta \hat{\mathbf{x}}_k + n_g \\ \mathbf{H}_g &= \frac{-1}{\|{}^G \hat{\mathbf{g}}_r\| \Delta t} \begin{bmatrix} ({}^G \hat{\mathbf{g}}_r \times {}^G \hat{\mathbf{v}}_{I_{k+1}})^\top & -{}^G \mathbf{g}^\top & \mathbf{0} & \mathbf{0} & \mathbf{0} \end{bmatrix} \\ \mathbf{r}_g + \mathbf{H}_g \delta \hat{\mathbf{x}}_k &= -n_g \sim \mathcal{N}(0, R_g) \end{aligned} \quad (15)$$

Since $\dim(r_g) < \dim(\mathcal{M})$, the Kalman gain is computed differently as $\mathbf{K} = \mathbf{P} \mathbf{H}^\top (\mathbf{H} \mathbf{P} \mathbf{H}^\top + \mathbf{R})^{-1}$. Apart from this difference, the process remains similar to the first update.

V. EXPERIMENT

A. Datasets and Evaluation Metric

We evaluated GaRLIO on three datasets: NTU4DRadLM [23], which uses a solid-state LiDAR, and Snail-Radar [24] and *Fog-Filled hallway* [11], both employing spinning LiDARs. NTU4DRadLM, collected using handcart and car in semi-structured environments, includes *loop** sequences with significant elevation changes. Snail-Radar, collected with handheld devices, e-bikes, and SUVs in adverse weather like heavy rain, presents high dynamics in structured environments. *Fog-Filled hallway*, gathered by drone in a geometrically uninformative area, was used only for gravity evaluation due to the lack of ground truth.

We compared GaRLIO with the three state-of-the-art LIOs: FAST-LIO2 [1], Point-LIO [3], and DLIO [25]. Although it would be ideal to compare our method with other radar-LiDAR-Inertial odometry approaches such as DR-LRIO [11], the unavailability of their code has precluded such evaluations. Consequently, we selected our comparison targets from established LIO algorithms.

We computed the root mean square error (RMSE) of the Absolute Trajectory Error (ATE) using evo [26], with translation errors in meters and angular errors in degrees. Results are **bold** for best, and underlined for second best. Legends for Fig. 5 and Fig. 6 are the same as in Fig. 4.

B. Evaluation on Velocity-aware Gravity Estimation

We performed a comparative analysis between our velocity-aware gravity estimation method and velocity-ignorant approach that utilizes double integration. The evaluation was performed across different platforms, including Unmanned Ground Vehicle (UGV) (*loop2*), and drone

TABLE II: NTU4DRadLM Dataset Evaluation

| | | Fast LIO2 | Point LIO | DLIO | GaRLIO |
|--------------|------------------|--------------|--------------|--------------|--------------|
| <i>cp</i> | ATE _t | 0.103 | 0.162 | 0.174 | 0.107 |
| | ATE _r | 0.574 | <u>0.706</u> | 1.697 | 0.750 |
| <i>nyl</i> | ATE _t | 1.259 | 0.507 | 1.214 | 0.973 |
| | ATE _r | <u>0.996</u> | 0.722 | 1.688 | 1.454 |
| <i>loop3</i> | ATE _t | 11.94 | 9.548 | 8.332 | 4.271 |
| | ATE _r | <u>1.714</u> | 2.082 | <u>2.101</u> | 1.496 |
| <i>loop2</i> | ATE _t | 15.81 | 20.27 | 10.38 | 3.976 |
| | ATE _r | <u>2.176</u> | 4.188 | <u>2.525</u> | 1.043 |

-- Ground Truth GaRLIO DLIO FAST-LIO2 Point-LIO

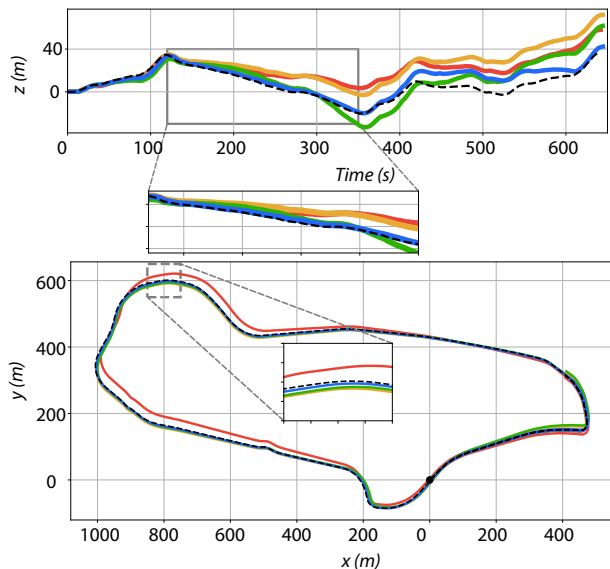


Fig. 4: Estimated z (top) and xy (bottom) trajectory for the *loop3* sequence. **Top**: From 120 to 350 seconds, GaRLIO accurately predicts elevation during the downhill descent, outperforming other methods. **Bottom**: GaRLIO results closely match the ground truth. The black dot represents the start point.

(*Fog-Filled hallway*). For gravity evaluation, we measured the deviation from the ground truth using the \square operation on \mathcal{S}^2 [16]. The global gravity ground truth is obtained through stationary initialization. As illustrated in Fig. 3, our method exhibits robust gravity estimation results, maintaining minimal deviation. The disparity between velocity-ignorant and velocity-aware methods is more significant on the UGV platform. UGV introduces significant bias and noise in IMU measurements arise from contact friction. These errors are exacerbated due to double integration, thus resulting in inaccuracy. In conclusion, our velocity-aware approach is more feasible for predicting gravity.

The effect of leveraging radar measurements on gravity estimation is depicted in Table. I. Exploiting velocity updates with radar measurement consistently enhances the accuracy of estimated gravity, thus highlighting the effectiveness of radar measurement in gravity estimation.

C. NTU4DRadLM Dataset

The evaluation results for the NTU4DRadLM dataset are shown in Table. II. In the *loop2* and *loop3* sequences, where data were collected using a car, our method outperformed other LIO methods in both translation and rotation. Fig. 4 shows the qualitative results in *loop3*. While other baselines show degraded performance due to steep uphill and downhill

TABLE III: Snail Radar Dataset Evaluation

| | | Fast LIO2 | Point LIO | DLIO | GaRLIO |
|-------------|------------------|-----------|-----------|--------------|--------------|
| <i>sl</i> | ATE _t | 14.34 | 10.98 | <u>5.054</u> | 1.059 |
| | ATE _r | 3.318 | 3.321 | <u>2.718</u> | 1.170 |
| <i>if</i> | ATE _t | 5.747 | 9.018 | 0.308 | 0.450 |
| | ATE _r | 1.479 | 3.291 | <u>0.730</u> | 0.591 |
| <i>iaf</i> | ATE _t | 24.99 | 73.19 | <u>6.192</u> | 4.672 |
| | ATE _r | 2.826 | 9.542 | <u>1.560</u> | 1.539 |
| <i>iaef</i> | ATE _t | 30.26 | 90.81 | <u>15.86</u> | 6.450 |
| | ATE _r | 3.317 | 9.004 | <u>1.436</u> | 1.397 |

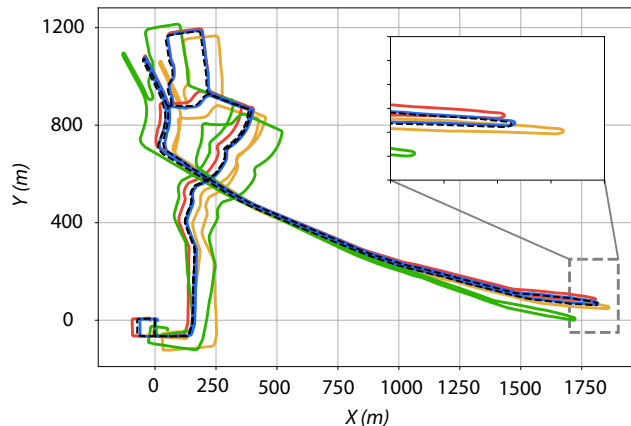


Fig. 5: Estimated trajectory for the *iaef* sequence and GaRLIO demonstrated superior performance over such a long sequence.

segments, GaRLIO achieves accurate estimation results in such challenging scenarios. This exhibits the robustness of our velocity-aware gravity estimation, even with significant elevation changes. However, in *nyl*, Point-LIO achieved the best performance. In *nyl*, the data was collected using a handcart, which causes significant vibrations. Point-LIO effectively handles these noisy measurements by estimating acceleration and angular velocity as part of the state. GaRLIO is not specifically designed for such conditions, although it achieves comparable performance.

D. Snail-Radar dataset

As shown in Table. III and Fig. 5, our method outperforms other LIO algorithms throughout the experiments. Specifically, in the *sl* sequence, other baselines exhibit significant errors in the z -axis due to the vigorous dynamic movements of the e-bike as shown in Fig. 6. Additionally, the Snail-Radar dataset contains various dynamic objects, such as vehicles and pedestrians, which affected the state predictions of FAST-LIO2 and Point-LIO, leading to degraded RMSE performance. Conversely, GaRLIO effectively mitigates drift in the roll and pitch directions through the velocity-aware gravity residuals, resulting in robust elevation estimation. Furthermore, GaRLIO successfully removes dynamic objects within the LiDAR by leveraging radar, as shown Fig. 7, resulting in more reliable performance compared to other methods. DLIO shows second-best performance across most sequences attributed to Geometric Observer and a continuous-time method. However, the absence of a dynamic handling mechanism and an update module based on velocity information reveals limitations along the experiments.

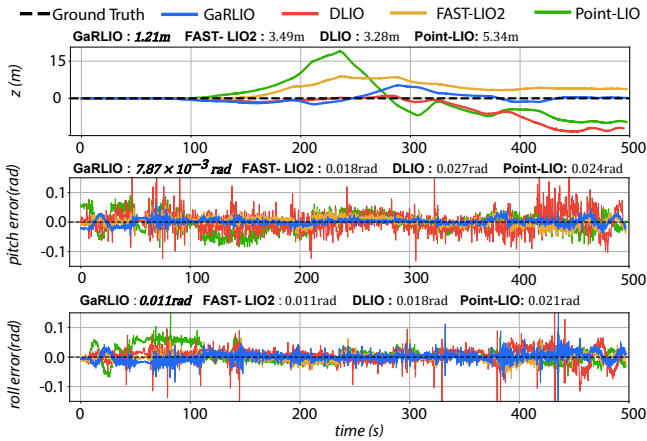


Fig. 6: z , pitch, and roll error in sl . The RMSE values for z , pitch, and roll are above each plot. Our method shows the lowest error along the baselines.

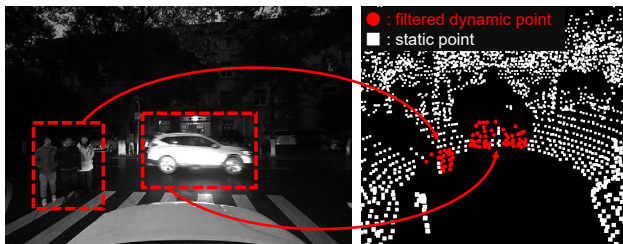


Fig. 7: Result of Dynamic removal module in Snail-Radar. The red points in the right LiDAR point cloud represent dynamic points that were removed using radar-based dynamic point.

E. Ablation Study

To evaluate the effect of each residual and dynamic removal module, we conducted experiments using various platforms, including a handcart (cp , nyl), a car ($loop2$, $loop3$), and an e-bike (sl). We created five variants by disabling two of the residuals ($g&v$) and Dynamic removal module (d): w/o $g&v&d$, w/o $g&v$, w/o v , w/o g , FULL, evaluated in terms of ATE.

1) *Effect of Velocity Residual*: As depicted in Table. IV, incorporating velocity residuals significantly enhances performance. This result corroborates the discussion in §V-B, demonstrating that incorporating velocity measurements facilitates more precise gravity estimation, thereby improving odometry estimation accuracy. Furthermore, the $loop3$ and $loop2$ sequences, which were collected using a car with higher speeds, demonstrate substantial improvements in state estimation through the incorporation of velocity residuals compared to cp , nyl , and sl , which are the slower sequences. This improvement is attributed to the inherent limitations of existing LIO methods that depend on kinematic models for velocity estimation, which are less accurate than our method at higher speeds.

2) *Effect of Gravity Residual*: When using gravity residuals without the addition of velocity measurements, a decline in performance was observed in $loop3$ and $loop2$, as indicated by the comparison between w/o $g&v$ and w/o v . As shown in Table. I, GaRLIO relies on the accuracy of the velocity for precise gravity estimation, which likely leads to performance degradation in the absence of velocity measurements. Accurate gravity estimation through velocity updates significantly improves odometry performance, as

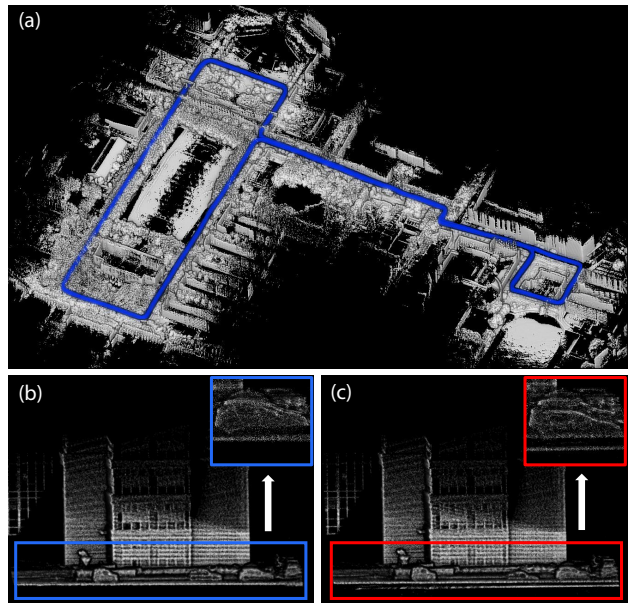


Fig. 8: (a) Mapping result of the if sequence generated using GaRLIO. Our method shows accurate alignment when revisiting previously traversed areas. At the revisited starting point: (b) With gravity residuals, ground regions are accurately aligned; (c) Without gravity residuals, vertical drift becomes apparent.

TABLE IV: Effect on ATE of Dynamic Removal Module and Each Residual

| | cp | $loop3$ | $loop2$ | nyl | sl |
|---------------|--------------|--------------|--------------|--------------|--------------|
| w/o $g&v&d$ | 0.101 | 12.44 | 9.163 | 1.281 | 1.889 |
| w/o $g&v$ | 0.115 | 10.83 | 8.573 | 1.280 | 1.467 |
| w/o g | 0.107 | 9.952 | 5.985 | 1.135 | 1.129 |
| w/o v | 0.098 | 11.28 | 11.17 | 0.991 | 1.194 |
| FULL | 0.107 | 4.271 | 3.976 | 0.973 | 1.059 |

demonstrated by the comparison between w/o g and FULL. These enhancements are particularly noticeable in elevation estimation, as seen in Fig. 8.

3) *Effect of Dynamic Removal Module*: The impact of the dynamic removal module can also be observed in Table. IV. Removing dynamic objects using radar point clouds improves performance in most sequences, with particularly notable enhancements in those containing numerous dynamic objects, such as $loop3$, $loop2$, and sl . These results demonstrate that the proposed algorithm is robust in environments with a high density of dynamic points.

VI. CONCLUSION

In this paper, we introduce GaRLIO, a gravity-enhanced radar-LiDAR-inertial odometry that provides a novel gravity estimation method that utilizes radar Doppler measurements. Differing from the velocity-ignorant approaches, our method ensures robust gravity estimation along the various platforms. Furthermore, the fusion of radar with LIO facilitates the dynamic removal within LiDAR point clouds. We validated its performance in public datasets, demonstrating its robustness even in challenging scenarios such as downhill and dynamic object-rich conditions. Remarkably, our approach represents superior improvements in mitigating vertical drift. GaRLIO, the first method to combine radar and gravity, is anticipated to establish new research directions for advancing robust SLAM systems based on UGV.

REFERENCES

- [1] W. Xu, Y. Cai, D. He, J. Lin, and F. Zhang, “FAST-LIO2: Fast direct lidar-inertial odometry,” *IEEE Trans. Robot.*, vol. 38, no. 4, pp. 2053–2073, 2022.
- [2] C. Qin, H. Ye, C. E. Pranata, J. Han, S. Zhang, and M. Liu, “LINS: A lidar-inertial state estimator for robust and efficient navigation,” in *Proc. IEEE Intl. Conf. on Robot. and Automat.*, 2020, pp. 8899–8906.
- [3] D. He, W. Xu, N. Chen, F. Kong, C. Yuan, and F. Zhang, “Point-LIO: Robust high-bandwidth light detection and ranging inertial odometry,” *Advanced Intelligent Systems*, vol. 5, no. 7, p. 2200459, 2023.
- [4] J. Laconte, S.-P. Deschênes, M. Labussière, and F. Pomerleau, “Lidar measurement bias estimation via return waveform modelling in a context of 3d mapping,” in *Proc. IEEE Intl. Conf. on Robot. and Automat.*, 2019, pp. 8100–8106.
- [5] V. Kubelka, M. Vaidis, and F. Pomerleau, “Gravity-constrained point cloud registration,” in *Proc. IEEE/RSJ Intl. Conf. on Intell. Robots and Sys.* IEEE, 2022, pp. 4873–4879.
- [6] Z. Wang, L. Zhang, Y. Shen, and Y. Zhou, “D-LIOM: Tightly-coupled direct lidar-inertial odometry and mapping,” *IEEE Trans. Multimedia*, vol. 25, pp. 3905–3920, 2023.
- [7] R. Nemiroff, K. Chen, and B. T. Lopez, “Joint on-manifold gravity and accelerometer intrinsics estimation for inertially aligned mapping,” in *Proc. IEEE/RSJ Intl. Conf. on Intell. Robots and Sys.* IEEE, 2023, pp. 1388–1394.
- [8] M. Ramezani, K. Khosoussi, G. Catt, P. Moghadam, J. Williams, P. Borges, F. Pauling, and N. Kottege, “Wildcat: Online continuous-time 3d lidar-inertial slam,” *arXiv preprint arXiv:2205.12595*, 2022.
- [9] A. Agha, K. Otsu, B. Morrell, D. D. Fan, R. Thakker, A. Santamaria-Navarro, S.-K. Kim, A. Bouman, X. Lei, J. Edlund *et al.*, “Nebula: Quest for robotic autonomy in challenging environments; team costar at the darpa subterranean challenge,” *arXiv preprint arXiv:2103.11470*, 2021.
- [10] C. Forster, L. Carlone, F. Dellaert, and D. Scaramuzza, “On-manifold preintegration for real-time visual-inertial odometry,” *IEEE Trans. Robot.*, vol. 33, no. 1, pp. 1–21, 2016.
- [11] M. Nissov, N. Khedekar, and K. Alexis, “Degradation resilient lidar-radar-inertial odometry,” in *Proc. IEEE Intl. Conf. on Robot. and Automat.*, 2024, pp. 8587–8594.
- [12] Y. Ma, X. Zhao, H. Li, Y. Gu, X. Lang, and Y. Liu, “RoLM: Radar on lidar map localization,” in *Proc. IEEE Intl. Conf. on Robot. and Automat.*, 2023, pp. 3976–3982.
- [13] Y. S. Park, J. Kim, and A. Kim, “Radar localization and mapping for indoor disaster environments via multi-modal registration to prior lidar map,” in *Proc. IEEE/RSJ Intl. Conf. on Intell. Robots and Sys.*, 2019, pp. 1307–1314.
- [14] H. Yin, R. Chen, Y. Wang, and R. Xiong, “RaLL: End-to-end radar localization on lidar map using differentiable measurement model,” *IEEE Trans. Intell. Transport. Sys.*, vol. 23, no. 7, pp. 6737–6750, 2022.
- [15] R. Hartley, M. Ghaffari, R. M. Eustice, and J. W. Grizzle, “Contact-aided invariant extended kalman filtering for robot state estimation,” *Intl. J. of Robot. Research*, vol. 39, no. 4, pp. 402–430, 2020.
- [16] D. He, W. Xu, and F. Zhang, “Kalman filters on differentiable manifolds,” *arXiv preprint arXiv:2102.03804*, 2021.
- [17] P. Shi, Z. Zhu, S. Sun, X. Zhao, and M. Tan, “Invariant extended kalman filtering for tightly coupled lidar-inertial odometry and mapping,” *IEEE/ASME Trans. Mechatronics*, vol. 28, no. 4, pp. 2213–2224, 2023.
- [18] Z. Yuan, J. Deng, R. Ming, F. Lang, and X. Yang, “SR-LIVO: Lidar-inertial-visual odometry and mapping with sweep reconstruction,” *IEEE Robot. and Automat. Lett.*, vol. 9, no. 6, pp. 5110–5117, 2024.
- [19] C. Doer and G. F. Trommer, “An ekf based approach to radar inertial odometry,” in *2020 IEEE International Conference on Multisensor Fusion and Integration for Intelligent Systems (MFI)*. IEEE, 2020, pp. 152–159.
- [20] J. Zhang, H. Zhuge, Z. Wu, G. Peng, M. Wen, Y. Liu, and D. Wang, “4DRadarSLAM: A 4d imaging radar slam system for large-scale environments based on pose graph optimization,” in *Proc. IEEE Intl. Conf. on Robot. and Automat.* IEEE, 2023, pp. 8333–8340.
- [21] Y. Cai, W. Xu, and F. Zhang, “ikd-tree: An incremental kd tree for robotic applications,” *arXiv preprint arXiv:2102.10808*, 2021.
- [22] T. Qin, P. Li, and S. Shen, “Vins-mono: A robust and versatile monocular visual-inertial state estimator,” *IEEE Trans. Robot.*, vol. 34, no. 4, pp. 1004–1020, 2018.
- [23] J. Zhang, H. Zhuge, Y. Liu, G. Peng, Z. Wu, H. Zhang, Q. Lyu, H. Li, C. Zhao, D. Kircali *et al.*, “Ntu4dradlm: 4d radar-centric multi-modal dataset for localization and mapping,” in *Proc. IEEE Intell. Transport. Sys. Conf.* IEEE, 2023, pp. 4291–4296.
- [24] J. Huai, B. Wang, Y. Zhuang, Y. Chen, Q. Li, Y. Han, and C. Toth, “Snail-Radar: A large-scale diverse dataset for the evaluation of 4d-radar-based slam systems,” *arXiv preprint arXiv:2407.11705*, 2024.
- [25] K. Chen, R. Nemiroff, and B. T. Lopez, “Direct lidar-inertial odometry: Lightweight lio with continuous-time motion correction,” in *Proc. IEEE Intl. Conf. on Robot. and Automat.*, 2023, pp. 3983–3989.
- [26] M. Grupp, “evo: Python package for the evaluation of odometry and slam.” <https://github.com/MichaelGrupp/evo>, 2017.